



## Wave Runup Loading Behind a Semipermeable Obstacle

Mayilvahanan Alagan Chella<sup>1</sup>; Andrew B. Kennedy, M.ASCE<sup>2</sup>; and Joannes J. Westerink<sup>3</sup>

**Abstract:** This paper describes an investigation of the interaction of breaking solitary wave runup with a two-dimensional semipermeable (vegetated) obstacle and the resulting wave loading on a downstream cylinder. The OpenFOAM model, together with an IHFOAM module for mangrove—fluid interaction, are used for 276 numerical experiments, performed for a wide range of damping coefficients. In general, wave heights inside and just downstream of the obstacle were found to increase, compared with the bare earth case, with reflection from and inside the obstacle as the major factor. By contrast, wave loads decreased strongly when sheltered by the obstacle, with increasing damping coefficients leading to lower loads, but with considerable scatter. This paper provides several different methods to estimate wave runup loads behind semipermeable obstacles, with results presented in forms that may prove useful for design. **DOI:** 10.1061/(ASCE) **WW.1943-5460.0000569**. © 2020 American Society of Civil Engineers.

**Author keywords:** Emergent semipermeable obstacle; Wave attenuation; Wave forces; Momentum flux; Runup loads; Computational fluid dynamics (CFD).

Introduction  $\varepsilon_D = F_D U \tag{2}$ 

Coastal protection structures, both natural and built, play a major role in reducing coastal flooding and storm damage by controlling hydrodynamics and decreasing loads on nearshore structures. One example of this type of process, and the subject of this paper, occurs when waves propagate through a semipermeable obstacle consisting of a group of emergent, rigid vertical cylinders, e.g., vegetation (Massel et al. 1999), closely spaced vertical piles (Dalrymple et al. 1988), permeable multiple-row pile breakwaters (Koftis et al. 2012), or a coastal forest (Shuto 1987). Hydrodynamic conditions behind these structures are altered from the no obstacle case, presumably decreasing wave heights, fluid velocities, and loads; this much is presumed but details of these reductions are not known with great confidence. Several theoretical and experimental studies have focused on modeling the wave scattering and dissipation by an array of emergent vertical cylinders (Wiegel 1961; Dalrymple et al. 1988; Kakuno and Nakata 1998; Mei et al. 2011; Koftis et al. 2012; Peruzzo et al. 2018). Coastal vegetation acts as a natural barrier between the land and sea, protecting landward coastal regions against extreme ocean events, including severe storms and tsunamis (Shuto 1987; Kandasamy and Narayanasamy 2005), through reflection from the vegetated mass, and by dissipation from leaves, stems, and roots. The drag force for a group of cylinders per unit base area and per unit cylinder length,  $F_D$ , can be directly related to the wave energy dissipation per unit area,  $\varepsilon_D$ , as follows (Dalrymple et al. 1984):

$$F_D = \frac{1}{2}C_D DNU|U| \tag{1}$$

<sup>3</sup>Dept. of Civil and Environmental Engineering and Earth Sciences, Univ. of Notre Dame, Notre Dame, IN 46556. Email: jjw@nd.edu

Note. This manuscript was submitted on May 17, 2019; approved on November 1, 2019; published online on April 13, 2020. Discussion period open until September 14, 2020; separate discussions must be submitted for individual papers. This paper is part of the *Journal of Waterway, Port, Coastal, and Ocean Engineering*, © ASCE, ISSN 0733-950X.

where  $C_D$  = drag coefficient; D = diameter of the element; N = number of drag elements per unit horizontal area; and U = horizontal fluid velocity. Based on the relationship between drag force and horizontal velocity [Eq. (1)], analytical solutions for the wave damping effect of a vegetation patch were developed for emergent rigid vegetation (e.g., Kobayashi et al. 1993) and flexible vegetation (e.g., Dubi and Torum 1994).

Several theoretical studies on wave attenuation in mangrove forests have been conducted for uniform (Massel et al. 1999) and varying (Vo Luong and Massel 2008) water depths. Nepf (1999) proposed a theoretical model to account for the vegetation induced drag, turbulence, and diffusion for emergent vegetation, based on vegetation density for flows with Reynolds' numbers Re > 200. It was found that turbulence intensity is mainly determined by the vegetation induced drag. Using a linear wave assumption for orbital velocities, Méndez et al. (1999) developed an analytical model to analyze wave induced hydrodynamics in a vegetated region of constant water depth and found that the analytical results were in good agreement with experimental data. Wave height attenuation, vegetation motion, and forces and moments on vegetation elements were analyzed for regular and irregular waves. Further, Mendez and Losada (2004) modified the vegetation induced wave damping relationship proposed by Dalrymple et al. (1984) to account for the energy dissipation due to random wave breaking and vegetation and seabed slopes. A detailed review of theoretical models for vegetation induced dissipation is presented in Chen and Zhao (2012).

Tanino and Nepf (2008) experimentally investigated a mean drag coefficient in a group of randomly distributed rigid cylinders in steady flow conditions. Augustin et al. (2009) investigated wave dissipation by emergent, near-emergent, rigid, and flexible vegetation through laboratory experiments and numerical simulations using the modified Boussinesq model COULWAVE (Cornell University Long and Intermediate Wave model). It was reported that emergent vegetation was found to have higher wave damping than near-emergent vegetation and that the wave attenuation and friction factors were quite unaffected by the motion of flexible elements. In the same way, the effects of stem density, incident wave height, and the model width on transmission, reflection coefficient,

<sup>&</sup>lt;sup>1</sup>Dept. of Civil and Environmental Engineering and Earth Sciences, Univ. of Notre Dame, Notre Dame, IN 46556 (corresponding author). ORCID: https://orcid.org/0000-0002-5462-966X. Email: malaganc@nd.edu

<sup>&</sup>lt;sup>2</sup>Dept. of Civil and Environmental Engineering and Earth Sciences, Univ. of Notre Dame, Notre Dame, IN 46556. Email: andrew.kennedy@nd.edu

and attenuation rate of a solitary wave propagating through an array of emergent rigid cylinders were studied numerically and experimentally by Huang et al. (2011) and Yang et al. (2017). Later, Hu et al. (2014) developed a method to determine drag coefficients for combined current and wave flow in submerged and emergent canopies based on laboratory measured data.

The application of Navier-Stokes equations with a k- $\varepsilon$  closure was proposed by Hiraoka and Ohashi (2008) to model plant canopy flows without considering the viscous stress term. The obtained empirical coefficients for the turbulent kinetic energy (k) and the turbulent dissipation rate  $(\varepsilon)$  were found to have a good agreement with measured field data. A nonhydrostatic Reynolds-averaged Navier-Stokes (RANS) model NHWAVE was developed by Ma et al. (2013) to investigate vegetation induced turbulence and nearshore circulation and wave attenuation under breaking and nonbreaking waves. Maza et al. (2013) applied a numerical model, IH-2VOF, based on the Navier-Stokes equations and the  $k-\varepsilon$  turbulence model for the interaction of regular waves with a submerged vegetation patch including plant motion. The model was able to capture wave attenuation and the velocity field of the obstructed flow inside and outside the vegetation. Later, Maza et al. (2015) modified the numerical approach and modeled the twodimensional vegetated flow problem by considering the macroscopic properties of the vegetated region, together with the coupling of the flow variables inside and outside the vegetation with IH-FOAM and OpenFOAM. The energy dissipation induced by an array of cylinders was represented as a drag force and added to the momentum equation to account for the loss due to the vegetation friction. The authors also performed a direct three-dimensional (3D) simulation of solitary wave propagation through an array of rigid vertical cylinders (Maza et al. 2015) and vegetation patches (Maza et al. 2016), including the flow field in the narrow passage between the cylinders. Large eddy simulations were carried out to model the flow features around an array of submerged rigid cylinders by Stoesser et al. (2009) and the vertical variation of forces on emergent cylinders for a wide range of flow conditions by Chakrabarti et al. (2016). The authors of both these studies benchmarked their numerical models against the experimental data reported by Lin (2008), who conducted an experimental campaign to examine the flow characteristics, including longitudinal and vertical variations of velocity and turbulence intensity. Furthermore, Chen et al. (2016) made an attempt to predict the wave transmission coefficient based on numerical simulations with the RANS equations and the RNG k– $\varepsilon$  model.

Several numerical studies have been attempted to model wave dissipation, flow characteristics, and turbulence intensities induced by emergent, rigid vegetation and an array of vertical cylinders for mostly nonbreaking regular and solitary waves. For instance, the flow problem of a breaking wave interacting with a semipermeable obstacle consists of two dissipation mechanisms: wave breaking and obstacle induced dissipation. Both mechanisms have been investigated experimentally (Blackmar et al. 2014) and theoretically (Mendez and Losada 2004; Vo Luong and Massel 2008; Henry and Myrhaug 2013; Myrhaug and Holmedal 2011) for random breaking waves in the frequency domain without explicitly modeling the wave breaking process. In addition, obstacle or vegetation induced reflection is also an important consideration, which has been disregarded in many theoretical investigations.

Several studies have focused on modeling vegetation induced wave attenuation and energy dissipation of nonbreaking regular waves in varying water depths. In real-world scenarios, a breaking wave event is composed of different physical processes, from the formation of an unstable wave crest before breaking to the completely broken waves in the surf zone (Svendsen 1978). Further, broken

waves can surge up the beach as runup and impose large loads and impulses on nearshore structures and coastal buildings during storm events. Little attention has been given to modeling broken waves, i.e., broken bore interaction with semipermeable (vegetation) obstacles and structures. The present investigation aimed at assessing the relationship between semipermeable obstacle properties, the obstacle induced dissipation of broken wave runup, and the resulting wave loads on downstream structures. Particular emphasis is given to the assessment of runup loads on downstream structures for different flow scenarios behind the obstacle.

The main purpose of the present work is to investigate numerically the wave runup dissipation induced by a semipermeable obstacle, and the associated wave loads on a downstream square cylinder, using the open-source model OpenFOAM together with IHFOAM (mangrove—fluid interaction module). In this paper, the numerical model is first benchmarked against the laboratory water surface elevations reported by Huang et al. (2011) before and after the interaction of a solitary wave with a semipermeable obstacle. Next, a series of simulations is performed for solitary wave runup and transformation after encountering an emergent semipermeable obstacle, and the subsequent wave loading on a square cylinder. A total of 276 simulations are performed for a wide range of damping coefficients.

# Properties of a Semipermeable Obstacle and Wave Damping Effect

The bulk drag coefficient  $C_D$  is an empirical factor relating the drag, flow velocity, fluid properties, and properties of the obstacle. Many studies have investigated the relationship in oscillatory flow between  $C_D$  and dimensionless flow quantities, such as the Reynolds number Re and Keulegan-Carpenter (KC) number (KC = VT/R), where V = characteristic velocity; T = wave period; and R = characteristic diameter of the object being loaded); see, e.g., Kobayashi et al. (1993), Mendez and Losada (2004), and Anderson and Smith (2014). Løvås and Tørum (2001) showed that the bulk drag coefficient of a specific plant or element can be described in terms of the local KC number; however, according to Kobayashi et al. (1993) and Méndez et al. (1999), the drag coefficient is also dependent on Re. Later, Mendez and Losada (2004) introduced an average drag coefficient ( $C_D$ ) based on a modified KC number along with the relative vegetation height. Based on Dalrymple et al. (1984), Maza et al. (2016) obtained an attenuation coefficient that relates the obstacle properties and incident wave heights.

As proposed by Dalrymple et al. (1984), the wave damping coefficient ( $\alpha L$ ) depends on the macroscopic properties of the obstacle, such as the stem diameter (D), stem density per unit plan area (N), drag coefficient ( $C_D$ ), length of the obstacle (L), and on the initial wave height (H). The evolution of a regular wave height along the obstacle is then given by (Mendez and Losada 2004)

$$H(x) = H_0 \left[ \frac{1}{1 + \frac{\alpha x}{3\pi}} \right] \tag{3}$$

where  $H_0$  = wave height at the beginning of the obstacle; x = distance into the semipermeable obstacle; and  $\alpha$  = damping factor. which can be simplified in the shallow water limit as

$$\alpha = DC_D N \frac{H_{\nu}}{d} \frac{H_0}{d} \tag{4}$$

J. Waterway, Port, Coastal, Ocean Eng.

where  $H_{\nu}$  = height of the stem vegetation, with a maximum value of  $H_{\nu}/d = 1.0$ . We do note that Mendez and Losada (2004) assumed small-amplitude waves interacting over a constant water depth, which is considerably different from the case studied herein.

For the present study, a semipermeable obstacle is placed on a flat shelf above the still water level, and is impacted by solitary wave runup. Thus, in this particular case, the runup wave height impacting the obstacle will be functionally equivalent to the water depth and thus  $H_0/d=1$  in Eq. (4). For the emergent vegetation considered in all cases here, we also find  $H_v/d=1$  in Eq. (4), and the final form can be simplified to

$$\alpha = DC_D N \tag{5}$$

Thus, the dimensionless damping coefficient,  $\alpha L$  only depends on knowable parameters of the obstacle in the runup region, or rather on combinations of those parameters as defined in Eq. (5). The most important thing to remember is that individual vegetation or obstacle properties are less important than the overall dissipation  $\alpha L$ . The damping coefficient ( $\alpha L$ ) provides a good representation of the main physical characteristics of an obstacle (vegetation) that includes all four different macroscopic properties. This is the only parameter adapted from Mendez and Losada (2004) that was considered as the measure of obstacle induced dissipation.

## **Computational Approach**

An open-source computational fluid dynamics (CFD) model (Open-FOAM), together with an IHFOAM module for mangrove—fluid interaction, (Maza et al. 2015) was utilized to model the interaction of waves with a semipermeable structure. In the numerical wave tank, the incompressible two-phase (air and water) flow is governed by the RANS equations, as modified for two-phase motion

$$\frac{\partial u_i}{\partial x_i} = 0 \tag{6}$$

$$\frac{\partial \rho u_i}{\partial t} + u_j \frac{\partial \rho u_i}{\partial x_j} - \frac{\partial}{\partial x_j} \left( \mu_{\text{eff}} \frac{\partial u_i}{\partial x_j} \right) = \frac{\partial p^*}{\partial x_i} - g_i x_j \frac{\partial \rho}{\partial x_i}$$
 (7)

where  $u_i$  = time-averaged velocity (i = 1, 2, 3 are three Cartesian components);  $p^*$  = pressure in excess of hydrostatic pressure;  $\rho$  = fluid density;  $\mu_{\text{eff}}$  = effective dynamic viscosity [which includes the effects of dynamic molecular viscosity ( $\mu$ ) and turbulent kinematic viscosity ( $\nu_{\text{turb}}$ )]; and  $g_i$  = gravitational acceleration ( $g_1$  = 0,  $g_2$  = 0,  $g_3$  = -9.81 m/s<sup>2</sup>).

The model for the motion of the air—water interface follows that of Hirt and Nichols (1981), which is based on a volume fraction ( $\beta$ ) with limits  $\beta = 1$  for a cell filled only with water, and  $\alpha = 0$  for a cell filled only with air. The volume fraction then evolves as

$$\frac{\partial \beta}{\partial t} + \frac{\partial u_i \beta}{\partial x_i} + \frac{\partial u_{c,i} \beta (1 - \beta)}{\partial x_i} = 0$$
 (8)

where  $u_{c,i}$  is a relative velocity. Further, the variation of the fluid properties in space, such as  $\mu$  and  $\rho$ , at a cell with both air and

water is given as

$$\Phi = \beta \Phi_{\text{water}} + (1 - \beta) \Phi_{\text{air}} \tag{9}$$

where  $\Phi$  is a dummy property.

The present computational approach is based on a macroscopic approach (Hiraoka and Ohashi 2008; Maza et al. 2015), which considers the bulk properties of a semipermeable structure; individual stems or cylinders are not modeled but rather their integrated effects. These macroscopic governing equations for fluid flow through the semipermeable obstacle can be derived by volume-averaging the continuity and momentum equations over a representative control volume. By assuming that the stems present in the obstacle are uniform rigid smooth cylinders, the change in the forward momentum due to the interaction of the flow with the obstacle can be modeled by the Morison equation for general unsteady flow, i.e., with the drag and inertia forces. The resulting equations for the mean flow averaged over the control volume are the volume-averaged Reynolds-averaged Navier-Stokes (VARANS) equations

$$\frac{\partial \langle u_i \rangle}{\partial x_i} = 0 \tag{10}$$

$$\frac{\partial \rho \langle u_i \rangle}{\partial t} + \langle u_j \rangle \frac{\partial \rho \langle u_i \rangle}{\partial x_j} - \frac{\partial}{\partial x_j} \left( \langle \mu_{\text{eff}} \rangle \frac{\partial \langle u_i \rangle}{\partial x_j} \right) 
= \frac{\partial \langle p^* \rangle}{\partial x_i} - g_i x_j \frac{\partial \langle \rho \rangle}{\partial x_i} - F_{D,i} - F_{I,i}$$
(11)

where  $\langle u_i \rangle$  = volume-averaged velocity (i = 1, 2, 3 are three Cartesian components);  $\langle \rho \rangle$  = volume-averaged fluid density;  $\langle p^* \rangle$  = volume-averaged pressure;  $\mu_{\rm eff}$  = effective dynamic viscosity;  $F_{D,i}$  = drag force; and  $F_{I,i}$  = inertia force

$$F_{D,i} = \frac{1}{2} \langle \rho \rangle C_D DN \langle u_i \rangle |\langle u_i \rangle| \tag{12}$$

$$F_{I,i} = \langle \rho \rangle C_M \frac{\pi D^2}{4} DN \frac{\partial \langle u_i \rangle}{\partial t}$$
 (13)

where D= diameter of a stem or element;  $C_D=$  drag coefficient; and  $C_M=$  inertia coefficient. The fluid flow outside the semipermeable obstacle is governed by the RANS equations [Eq. (7)], whereas the flow field inside the obstacle is described by the VAR-ANS equations [Eq. (11)]. By using the control volume mean flow quantities, which are continuous across the interface, the flow field variables, such as velocity and pressure, are linked for the fluid flow inside and outside the semipermeable obstacle. However, the turbulent production within the obstacle is modeled using a modified two-equation  $k-\varepsilon$  turbulence model, as proposed by Hiraoka and Ohashi (2008), and with slightly different closure coefficients, as presented by Maza et al. (2013)

$$\frac{\partial k}{\partial t} + \langle u_i \rangle \frac{\partial k}{\partial x_j} = \frac{\partial}{\partial x_j} \left[ \langle \nu_{\text{eff}} \rangle \frac{\partial k}{\partial x_j} \right] + \langle \nu_t \rangle \frac{\partial \langle u_i \rangle}{\partial x_j} \left( \frac{\partial \langle u_i \rangle}{\partial x_j} + \frac{\partial \langle u_j \rangle}{\partial x_i} \right) \\
- \varepsilon + C_{kp} C_D D N \sqrt{\langle u_i \rangle \langle u_j \rangle k} \tag{14}$$

$$\frac{\partial \varepsilon}{\partial t} + \langle u_i \rangle \frac{\partial \varepsilon}{\partial x_j} = \frac{\partial}{\partial x_j} \left[ \left( \frac{\langle \nu_t \rangle}{\sigma_{\varepsilon}} + \langle \nu \rangle \right) \frac{\partial \varepsilon}{\partial x_j} \right] + C_{\varepsilon 1} \frac{\varepsilon}{k} \langle \nu_t \rangle \frac{\partial \langle u_i \rangle}{\partial x_j} \left( \frac{\partial \langle u_i \rangle}{\partial x_j} + \frac{\partial \langle u_j \rangle}{\partial x_i} \right) - C_{\varepsilon 2} \frac{\varepsilon^2}{k} + C_{\varepsilon p} C_D D N \sqrt{\langle u_i \rangle \langle u_j \rangle \varepsilon}$$
(15)

where k= turbulent kinetic energy; and  $\varepsilon=$  dissipation rate. The closure coefficients  $\langle v_{\rm eff} \rangle$ ,  $\langle v_t \rangle$ ,  $C_{\varepsilon 2}$ ,  $\sigma_{\varepsilon}$ ,  $C_{kp}$ , and  $C_{\varepsilon p}$  are 0.09 m<sup>2</sup>/s, 1.44 m<sup>2</sup>/s, 1.92, 1.30, 1.0, and 3.5, respectively.

In general, RANS equations are based on the time-averaged conservation of mass and momentum of the flow field. The turbulent stress is modeled using a two-equation model, k– $\varepsilon$  turbulence model, which is based on the Boussinesq hypothesis. In fact, the turbulence production is overestimated for highly strained flow as it depends linearly on the strain rate of mean flow, resulting in removal of excess energy from the mean quantities. Additional turbulent stresses emerge from larger mean velocity fluctuations and momentum exchange at the free surface (interface), leading to overprediction of turbulence levels. Moreover, the RANS equations do not solve 3D turbulent structures, but they model the time average effects of turbulent fluctuations. Overall, the RANS equations can provide reasonable approximations of the time-averaged turbulent flow properties in high-Reynolds-number flows through complex solid boundaries (Alagan Chella et al. 2016).

## **Computational Domain and Convergence Study**

The computational domain is given at laboratory scale, and is 0.35 m wide and 1.60 m high with an offshore water depth of 0.35 m. It is composed of a 1/10 slope followed by a flat shelf at a height of 0.40 m above the offshore bed. A semipermeable obstacle is located 0.3 m landward from the beginning of the flat section; a square cylinder is then placed behind the obstacle, as shown in Fig. 1. At the inlet, a Dirichlet boundary condition defines the wave surface elevation ( $\eta$ ) and the velocity components (u, v, w). Solitary waves used in this study are based on Boussinesq theory (Lee et al. 1982). The tank bottom and the cylinder surface are represented as walls with no slip condition and sides are considered as walls with slip condition. Both the left and right boundaries are far enough from the area of interest that any reflected waves arising from them will not affect the important parts of the simulations.

The local mesh refinement technique is used in this study and the grid size in all three directions is  $0.005 \,\mathrm{m}$  (i.e.,  $dx = dy = dz = 0.005 \,\mathrm{m}$ ) in the flow region of interest. A numerical convergence study was carried out using four different grid sizes ( $\Delta x = 0.020$ , 0.010, 0.005, and 0.003 m). Here, a solitary wave based on Boussinesq theory (Lee et al. 1982) with height 0.10 m propagates through the domain, encounters the semipermeable obstacle, and interacts with a rectangular cylinder, as shown in Fig. 1. Along the tank,

six wave gauges were specified, as shown in Fig. 1. Fig. 2 shows the computed wave surface elevations ( $\eta$ ) at  $x=1.00\,\mathrm{m}$  (WG-2), 6.0 m (WG-5), and 6.8 m (WG-6) and the force impulse on the cylinder as a function of time. Near the offshore boundary, wave surface elevations for different  $\Delta x$  are close to identical as the wave is undisturbed. The wave then shoals as it propagates over the sloping seabed; the wave increases in height and breaks before reaching the flat shelf. The wave runup then passes through the semipermeable obstacle and interacts with the square cylinder. The water levels at the seaward edge of and inside the obstacle increase moderately, owing to wave reflections offshore from the obstacle. This causes an increase in water level at the landward edge of the obstacle ( $x=6.8\,\mathrm{m}$ ) compared with the water level at  $x=6.0\,\mathrm{m}$ . A detailed analysis of the numerical results was performed for different grid sizes to evaluate convergence.

Richardson extrapolation (Richardson and Gaunt 1927) using successive grid resolutions was used to estimate quantities for a grid size approaching zero ( $\Delta x \rightarrow 0$ ). According to Roache (1994), numerical solutions converge monotonically for convergence ratios R < 1. As shown in Table 1, R is less than 0.3, which is well below the threshold value for all the wave gauge locations along the tank and the force impulse. The extrapolated solution at  $\Delta x = 0$ , the order of convergence ( $r^p$ ), and the convergence group indices (CGI<sub>21</sub> and CGI<sub>32</sub>) for the combination of three grids ( $\Delta x = 0.05$ , 0.010, and 0.020 m) are calculated as follows:

$$f_{\Delta x=0} \approx f_1 + \left[ \frac{f_1 - f_2}{r^p - 1} \right]$$

$$r = \Delta x_{\text{grid2}} / \Delta x_{\text{grid1}} = \Delta x_{\text{grid3}} / \Delta x_{\text{grid2}} = 2.0$$
(16)

$$p = \frac{\ln(\epsilon_{32}/\epsilon_{21})}{\ln(r)}$$

$$\epsilon_{i+1,i} = f_{i+1} - f_i$$

$$R = \frac{\epsilon_{21}}{\epsilon_{32}}$$
(17)

$$CGI_{i+1,i} = F_s \frac{|\epsilon_{i+1,i}|}{f_i(r^p - 1)}$$
 (18)

where  $f_{\Delta x=0}$  = exact solution;  $f_1$  = numerical solution of grid 1;  $f_2$  = numerical solution of grid 2;  $r^p$  = order of convergence; and r = refinement ratio. It is apparent from the grid convergence study that the grid size  $\Delta x = 0.005$  m gives a reasonable estimate of the wave

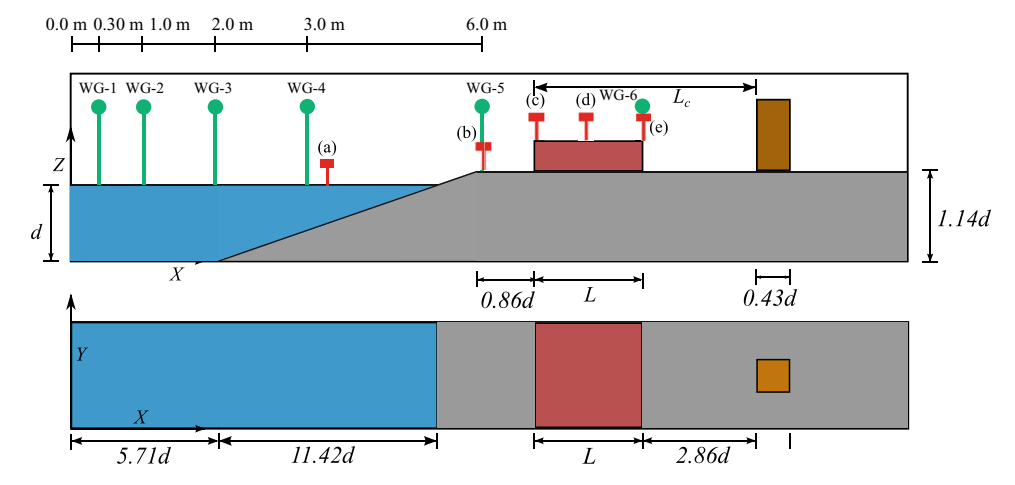
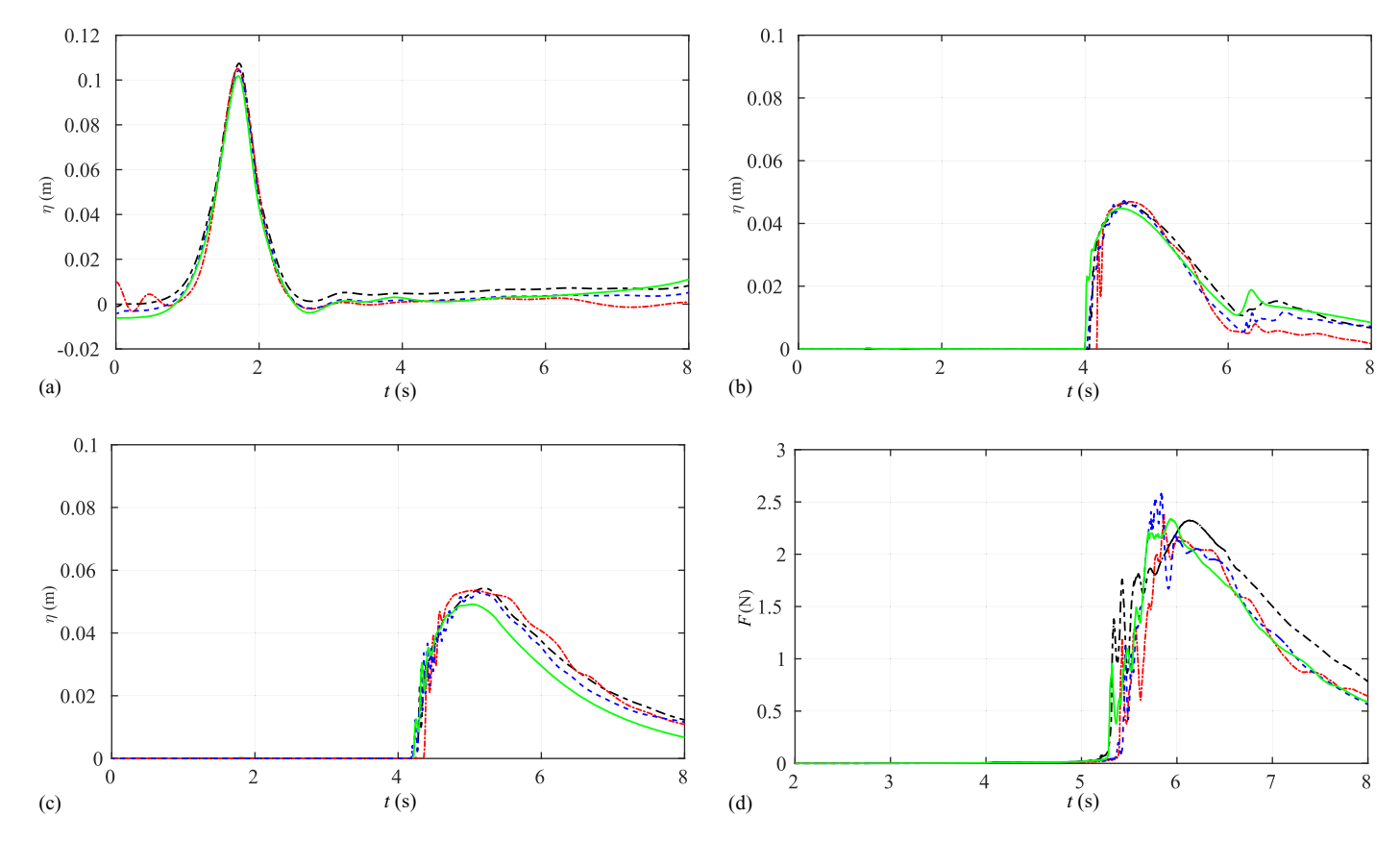


Fig. 1. Cross-sectional and plan views of computational setup: wave gauge locations from (a) upstream to (e) downstream of the obstacle are specified as square markers for the wave evolution case (Fig. 5).



**Fig. 2.** Comparison of (a–c) computed wave surface elevations ( $\eta$ ) at (a) x = 1.0 m (WG-2); (b) x = 6.0 m (WG-5); (c) x = 6.8 m (WG-6); and (d) computed wave force as a function of time for four different grid sizes. Thick dashed line:  $\Delta x = 0.003$  m; dash-dot line:  $\Delta x = 0.005$  m; thin dashed line:  $\Delta x = 0.010$  m; and solid line:  $\Delta x = 0.020$  m.

**Table 1.** Computed wave surface elevations ( $\eta$ ) at different locations along the wave tank, force impulse on the downstream square cylinder, and the convergence parameters for four different grid sizes

Grid sizes (m)	x = 0.3  m (WG-1)	x = 1.0  m (WG-2)	x = 2.0  m (WG-3)	x = 3.0  m (WG-4)	x = 6.0  m (WG-5)	x = 6.8  m (WG-6)	Force impulse (Ns)
0.020	0.10460	0.10170	0.09900	0.10270	0.04507	0.04918	3.660
0.010	0.10760	0.10420	0.10330	0.10630	0.04672	0.05322	3.624
0.005	0.10910	0.10510	0.10386	0.10660	0.04692	0.05354	3.616
0.003	0.10940	0.10524	0.10387	0.10660	0.04693	0.05360	3.618
0.000 (RE)	0.10960	0.10537	0.10386	0.10662	0.04695	0.05356	3.613
$CGI_{32}/r^pCGI_{12}$	1.007	1.005	1.002	1.004	1.006	1.004	0.997
Convergence ratio $(R)$	0.13	0.11	0.08	0.11	0.12	0.08	0.21
Error band (%)	1.84	1.11	0.54	0.31	0.49	0.65	-0.28

surface elevations and force impulse compared with the extrapolated solution at  $\Delta x = 0$ , with an error band ranging between 1.84% and -0.28%. In addition, the  $CGI_{32}/r^{p}CGI_{12}$  ratio is very close to 1, implying that the numerical solutions are well within the asymptotic range of convergence. Therefore, the grid size  $\Delta x = 0.005$  m is selected for further numerical simulations.

## Validation Study

The numerical results are compared with the experimental data reported by Huang et al. (2011). In the benchmark case, a 1.635 m long semipermeable obstacle consisting of cylindrical elements of diameter D = 0.01 m at a density of N = 560 m<sup>-2</sup> is placed at a distance of 3.5 m from the inlet in a constant water depth of 0.15 m, as

shown in Fig. 3. In the numerical wave tank, the propagation of a 0.05 m high solitary wave through the obstacle was simulated and the computed wave surface elevations before and after the obstacle were compared with the experimental data (Huang et al. 2011). Fig. 4 shows a comparison of computed results and measured data for the water surface elevation before (WG-1) and after the obstacle (WG-2). As soon as the wave starts to interact with the obstacle, a portion of wave energy is reflected offshore, resulting in a slight increase in the wave height upstream, as seen in Fig. 4(a). Inside the obstacle, the wave height begins to attenuate through obstacle induced drag [Fig. 4(b)]. Numerical results are in good agreement with the measured data, indicating that the obstacle induced wave dissipation and the resulting wave height attenuation are well reproduced in the numerical wave tank.

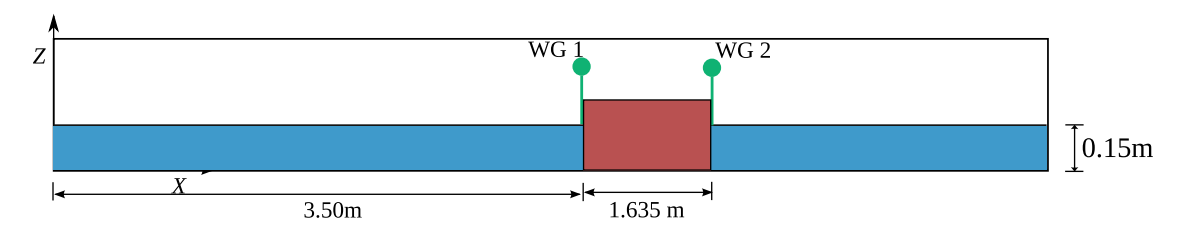


Fig. 3. Sectional view of computational setup for the validation study. (Data from Huang et al. 2011.)

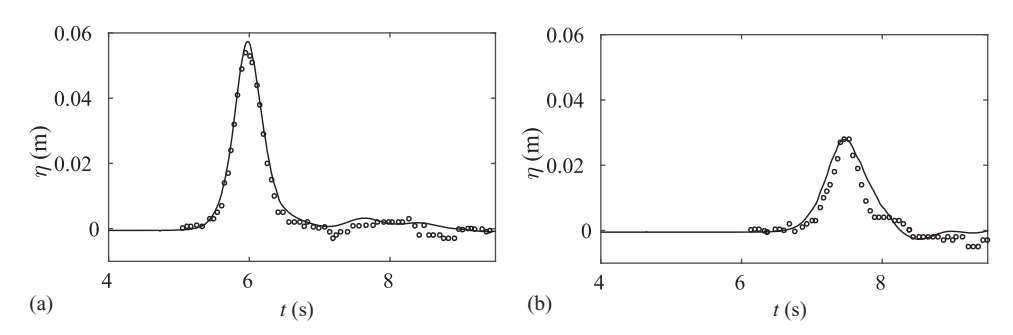


Fig. 4. Comparison of computed results and experimental data: (a) x = 3.50 m (WG-1); and (b) x = 5.135 m (WG-2). Circles: experimental data; solid lines: numerical results. (Data from Huang et al. 2011.)

#### **Dimensionless Parameters**

In the present study, a number of dimensionless parameters are used to provide an overview of how the physical parameters, including the properties of semipermeable obstacles and incident waves, are related to each other and their effect on the wave forces

$$\eta_{\text{max}}^* = \frac{\eta_{\text{max}}}{\eta_{(\text{max})\text{up0}}}; \qquad \eta^* = \frac{\eta}{\eta_{(\text{max})\text{up0}}}$$
(19)

$$\alpha L = C_D NDL \tag{20}$$

$$H^{+} = \frac{H_a}{H_{b0}}; \qquad H^{*} = \frac{H_a}{H_{a0}}$$
 (21)

$$MF_{\text{max}}^* = \frac{MF_{\text{max}}}{MF_{(\text{max})\text{up0}}}; \qquad MF^* = \frac{MF}{MF_{(\text{max})\text{up0}}}$$
 (22)

$$M^* = \frac{MF_a}{MF_{a0}}; \qquad M^+ = \frac{MF_a}{MF_{b0}}$$
 (23)

$$MF = \int_{-d}^{d+\eta} \rho u^2 dz \tag{24}$$

$$MF_{NCP} = \int_{-d}^{d+\eta} P + \rho u^2 dz \tag{25}$$

$$F^* = \frac{F}{MF_{c0}W}; \qquad F_{NC0} = \frac{F_{\text{max}}}{MF_{c0}W}; \qquad F_{N0} = \frac{F_{\text{max}}}{F_0}$$
 (26)

$$F_{NC} = \frac{F_{\text{max}}}{MF_{NC}W}; \qquad F_{NCP} = \frac{F_{\text{max}}}{MF_{NCP}W}$$
 (27)

## **Results and Discussion**

In the present simulation, waves with four different heights break on the slope, runup over the flat shelf, and interact with a semipermeable obstacle and downstream cylinder. As listed in Table 2,

**Table 2.** Computational cases for test matrix

Description	Number of cases
No obstacle ( $\alpha L = 0$ ), no cylinder	4
Obstacle, no cylinder	128
No obstacle, cylinder	16
Obstacle, cylinder	128
Total cases	276

132 simulations were performed with no cylinder to investigate the influence of the semipermeable obstacle on hydrodynamic properties at the cylinder location. Next, 144 simulations were carried out with the cylinder in place for a total of 276 computational runs. These tests have a significant range of runup and damping conditions, yielding a range of hydrodynamics and loading at the cylinder location.

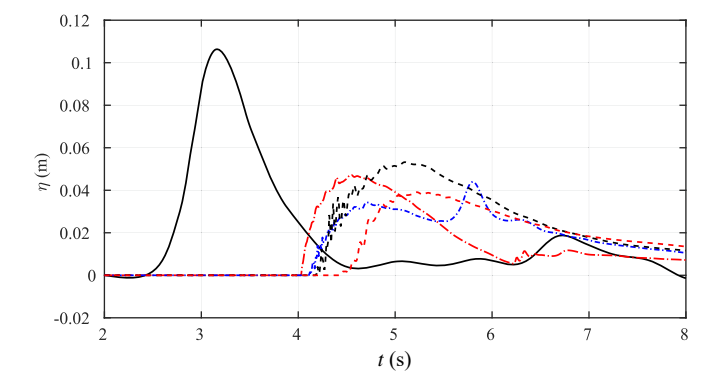
#### Influence of Semipermeable Obstacle on Runup

In this section, the effects of a semipermeable obstacle on wave runup depths are examined in the absence of the cylinder. First, selected examples are shown that demonstrate the obstacle's effects on water surface elevation over time. Next, examples of water surface envelopes are shown to demonstrate the variation of the maximum runup height along the tank. Finally, wave runup depths before and after the obstacle are compared with values at the same locations for the bare earth case.

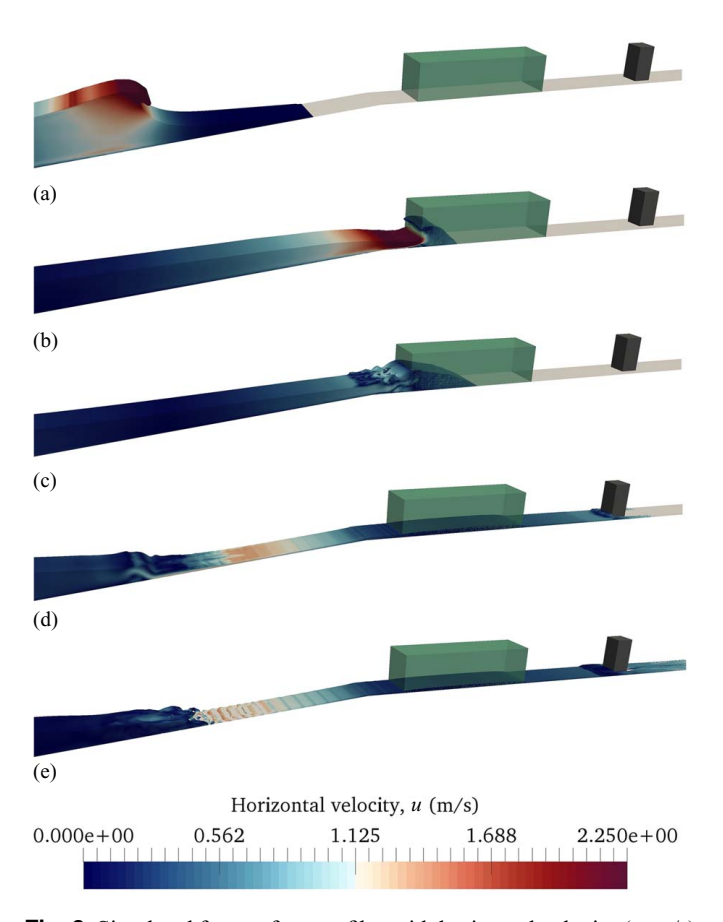
## **Example Time Series of Wave Evolution**

Fig. 5 shows the computed time series of free surface elevation at different locations along the wave tank from the wave generation zone to the downstream side of the semipermeable obstacle (Fig. 1). A solitary wave with height  $H_0/d = 0.26$  is generated at a constant water depth of 0.35 m and grows higher and steepens as it propagates over a slope, owing to shoaling. Fig. 6 presents the simulated free surface profiles with horizontal velocity (u) at times t = 2.30, 3.15, 3.65, and 7.91 s. The wave steepening continues until it breaks on

J. Waterway, Port, Coastal, Ocean Eng.



**Fig. 5.** Wave surface elevation ( $\eta$ ) versus time for H/d = 0.26, L/d = 3.14,  $\alpha L = 44.60$  at (a) x/d = 11.40 (solid line); (b) x/d = 17.14 (thick dash-dot line); (c) x/d = 18.0 (thin dash-dot line, immediately before obstacle); (d) x/d = 19.57 (thick dashed line), inside obstacle); and (e) x/d = 21.14 (thin dashed line, immediately after obstacle). The computed wave gauge locations [(a)–(e)] are specified as square markers in Fig. 1.



**Fig. 6.** Simulated free surface profiles with horizontal velocity (u, m/s) for H/d = 0.26 and L/d = 3.14 at time t = (a) 2.30 s; (b) 3.15 s; (c) 3.65 s; (d) 6.90 s; and (e) 8.10 s.

the slope, as depicted in Fig. 6(a). After breaking, the wave height decreases shoreward as it propagates on the flat shelf [Fig. 6(b)]. The water level in front of (thin dash-dot line of Fig. 5, x/d = 18.0) and inside (thick dashed line of Fig. 5, x/d = 18.49) the obstacle increases slightly because of wave reflections, as shown in Fig. 6(c). These primary and reflected peaks can be seen from Fig. 5 (thin dash-dot line). In particular, the water level inside the obstacle at x/d = 18.49 is greater than that slightly seaward of the obstacle at x/d = 17.14.

Landward of the obstacle, the wave height (dashed line of Fig. 5, x/d = 19.42) decreases as illustrated in Fig. 6(d) as a result of energy dissipation.

#### **Maximum Wave Amplitude Envelope**

Figs. 7 and 8 show different aspects of wave evolution for incident solitary wave heights  $H_0/d = 0.26$ , 0.49 for two different damping coefficients and the bare earth case ( $\alpha L = 0$ ). In each figure, part (a) shows profiles of the water surface elevations along the length of the runup region, whereas parts (b) and (c), respectively, give time series of the surface elevations immediately before and immediately after the obstacle. The computed wave heights are normalized with the height at x/d = 17.14 (i.e., on the flat shelf just before the obstacle) to provide a runup scaling rather than an incident wave scaling [Eq. (19)]. For both incident wave heights with no obstacle ( $\alpha L =$ 0.0), the wave height after breaking decreases continuously as expected. Figs. 7(a) and 8(a) show similar trends for the flow through the sparsely vegetated obstacle ( $\alpha L = 0.60$ ), with slightly higher maximum surface elevations than for no obstacle ( $\alpha L = 0.0$ ). However, the flow is strongly altered for the densely populated stems  $(\alpha L = 133.80)$ : a large part of the wave is reflected, increasing the height greatly within the obstacle. Even at the landward end of the obstacle (x/d=21.20), the wave height has decreased greatly from the seaward side, but is still larger than that for  $\alpha L = 0.0$ . As can be seen from Figs. 7 and 8, the broken wave height attenuates continuously as it propagates shoreward on the flat shelf in the absence of the obstacle. Thus, the wave height at the seaward edge of the obstacle  $(H_b0)$  is always higher than the wave height at the landward edge of the obstacle  $(H_a0)$ . In fact, the longer the obstacle, the higher the rate of wave height reduction.

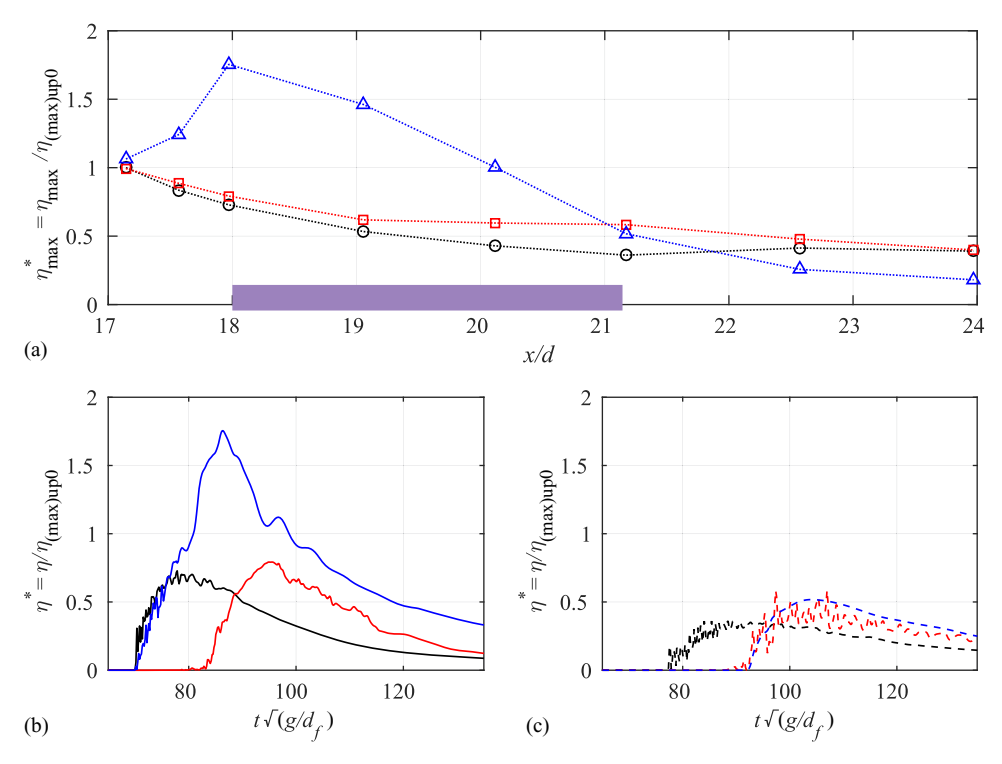
#### Wave Transformation through an Obstacle

Fig. 9 shows the normalized wave heights after the obstacle as a function of the normalized wave damping coefficient,  $\alpha L$ , for all cases given in Table 2. Two different wave height normalizations are presented, both based on the no vegetation ( $\alpha L=0$ ) case [Eq. (21)]. Normalization  $H^+=H_a/H_{b0}$  uses the wave height immediately before the obstacle location to normalize the wave height after the obstacle for many values of  $\alpha L$ . In contrast, normalization  $H^*=H_a/H_{a0}$  uses the wave height immediately after the obstacle location to normalize the wave height [Eq. (21)]. Both are valid, but represent different quantities:  $H^+$  gives the computed decrease in wave height after traveling through an obstacle compared with the upstream height, while  $H^*$  gives the relative decrease in height at this location if an obstacle were to be placed upstream of it.

The theoretical relation for the change in wave heights for shallow water, emergent vegetation, and a flat bed is given by Eq. (3). This was derived for regular waves over constant depth, not for wave runup, and as such is expected to have additional error for the present tests. However, it is easily computed and does provide a straightforward measure for comparison. The theoretical damping is plotted as a solid line in Fig. 9 for both normalized wave heights. Three observations are immediate.

- Almost all wave heights are much greater than those predicted by Eq. (3).
- Runup wave heights downstream of the obstacle show a very weak decrease with increasing damping coefficient,  $\alpha L$ .
- There is considerable scatter in the wave height ratios for a given  $\alpha L$ .

The very slow decrease in wave heights with increased predicted damping and lack of agreement with theory may seem unexpected, but may be partially explained by considering the assumptions in the original (Mendez and Losada 2004) theory, which is based on Dalrymple et al. (1984). In the theory of Mendez



**Fig. 7.** Computed (a) normalized maximum wave surface elevation  $\eta_{\text{max}}^*$  versus x/d along the semipermeable obstacle and normalized wave surface elevations ( $\eta^*$ ) (b) before and (c) after the obstacle versus  $t\sqrt{g/d_f}$  for  $H_0/d=0.26$  and  $\alpha L=0.0$ , 0.60, and 133.80. Thick solid and dashed lines:  $\alpha L=0.0$ ; medium solid and dashed lines:  $\alpha L=0.60$ ; and thin solid and dashed lines:  $\alpha L=133.80$ .

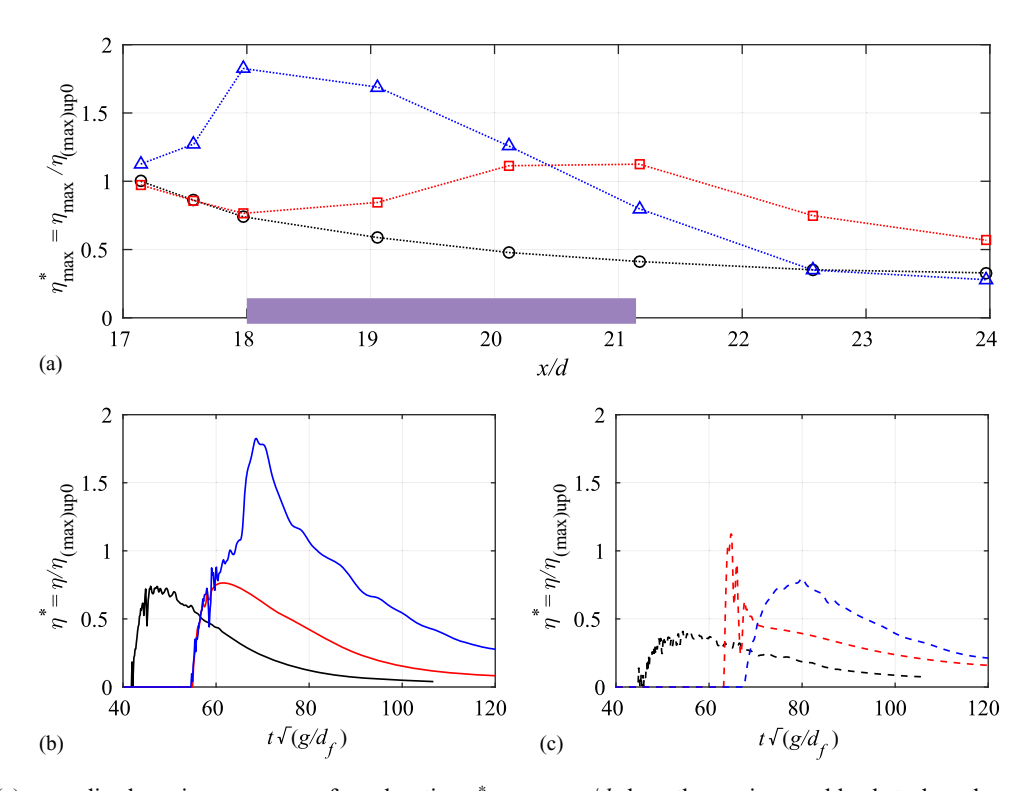
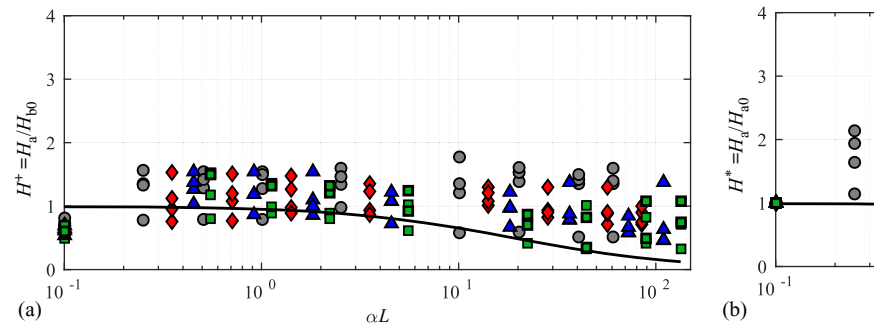


**Fig. 8.** Computed (a) normalized maximum wave surface elevation  $\eta_{\text{max}}^*$  versus x/d along the semipermeable obstacle and normalized wave surface elevations ( $\eta^*$ ) (b) before and (c) after the obstacle versus  $t\sqrt{g/d_f}$  for  $H_0/d=0.49$  and  $\alpha L=0.0, 0.60$ , and 133.80. The legends are the same as those defined in the caption of Fig. 7.

04020014-8

and Losada (2004), small-amplitude waves were assumed with vegetation flooded by a positive still water depth. None of these assumptions is true here: wave amplitudes are equal to water depths in the runup region, and mean depth is zero. The theory furthermore

implicitly assumes no wave reflection, which blatantly contradicts the present results. The reflections increase water levels at the seaward edge of the obstacle, which in turn increase wave heights inside the obstacle, with stronger damping leading to greater heights



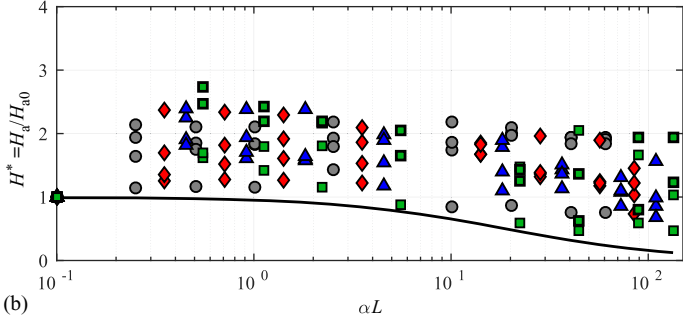


**Fig. 9.** Computed normalized wave heights: (a)  $H^+$ ; and (b)  $H^*$  versus  $\alpha L$  for different  $H_0/d$  and L/d = 1.43 (circles), 2.00 (diamonds), 2.58 (triangles), and 3.14 (squares). Solid line: theoretical values based on Mendez and Losada (2004). Values shown at  $\alpha L = 10^{-1}$  on the log scale are actually for  $\alpha L = 0$ .

at the seaward edge. This is a major reason why the theory overpredicts damping.

Following from the definition of  $H^*$ , magnitudes must be unity for  $\alpha L = 0$ , as the flow is undisturbed. However, Fig. 9(b) shows the highly counterintuitive result that, for low but nonzero  $\alpha L$ , the computed runup depths behind the obstacle are greater than if there were no obstacle at all. Reasons for this increase may be found in Figs. 7 and 8. The low dissipation case,  $\alpha L = 0.60$ , is seen to have a steep runup front, which is most evident for the larger incident height  $H_0/d = 0.49$ . It appears that the first effect of a low dissipation obstacle is to steepen the initial bore front by slowing down its tip, steepening the bore front and increasing runup depth behind the obstacle. However, we note that this does not mean that loads will increase, as will be shown shortly. In the case of strong damping ( $\alpha L = 133.8$ ), the wave propagation is significantly obstructed and a considerable amount of energy is reflected offshore, causing an increase in water level upstream (Figs. 5 and 7). However, higher energy dissipation in the obstacle greatly decreases these larger heights as the runup propagates through the obstacle. At the landward end, even though the wave heights for strong damping decrease greatly from their values at the seaward end, the large seaward heights arising from strong reflection mean that the downstream heights vary only weakly from the no damping or weak damping conditions. For the flow through the obstacle with  $\alpha L = 0.60$ , a relatively small wave damping occurs and, conversely, the water level at the shoreward edge of the obstacle is higher than in the bare earth case ( $\alpha L = 0$ ). In this case, the obstacle induced drag force slows the fluid slightly and induces partial reflection, causing a rise in water level at the shoreward edge of the obstacle. In the next section, the longitudinal variation and changes in the upstream and downstream momentum flux along the obstacle will be investigated for different flow conditions.

## Influence of a Semipermeable Obstacle on the Variation of Momentum Flux

This section examines the variation of momentum flux upstream and downstream of the obstacle and has two parts:

- the variation of maximum momentum flux along the tank, i.e., maximum momentum flux envelope for the selected cases;
- changes in momentum flux after the obstacle for all cases listed in Table 2.

## **Maximum Momentum Flux Envelope**

Figs. 10 and 11 show the changes in momentum fluxes ( $MF_{\rm max}^*$  and  $MF^*$ ) induced by the semipermeable obstacle, normalized with the maximum flux at x/d = 17.14 (i.e., on the flat shelf just before the

obstacle) [Eq. (22)] for the bare earth case. Envelopes for both wave heights  $H_0/d = 0.26$  and  $H_0/d = 0.49$  show *increases* in MF inside the obstacle, apparently arising from the large increase in water levels discussed in the previous section. After the obstacle, MF decreases for all cases, with the highest values found for the moderate damping cases using  $\alpha L = 0.60$ . Time series shown in Figs. 10(b and c) and 11(b and c) show significant steepening of the bore front and increased noise in the signal for the lightly damped case, but all MF values at the end of the obstacle are surprisingly similar, even for the highly damped cases. After the obstacles, however, MF for the highly damped case shows a significant decrease. These changes in MF will be compared with loading in the next section; although there are strong trends, there is not a perfect correlation.

#### Momentum Flux Transformation through the Obstacle

Here, two different normalizations were considered to describe the changes in the momentum flux for all cases presented in Table 2. Both normalizations examine  $MF_a$  after the obstacle. The quantity  $M^+ = MF_a/MF_{b0}$  normalizes this by  $MF_{b0}$  [Eq. (23)] immediately before the obstacle location for the bare earth case  $(\alpha L = 0)$ , while  $M^* = MF_a/MF_{a0}$  normalizes by the value after the obstacle for  $\alpha L = 0$ ,  $MF_{a0}$  [Eq. (23)]. Fig. 12(a) shows the change in the upstream and downstream normalized momentum flux  $(M^+)$  for all cases presented in Table 2. Again, several factors become readily apparent.

- For relatively low but nonzero damping of  $\alpha L < 2$ , peak momentum fluxes downstream of the obstacle *increase by factors of up to two over the bare earth case*.
- For stronger damping of  $\alpha L > 2$ , peak momentum fluxes decrease rapidly, and by  $\alpha L = 20$  are approximately 10%–30% of their bare earth values.
- Peak momentum fluxes of αL>100 are less than 10% of their bare earth values.
- For similar damping coefficients,  $\alpha L$ , the longest obstacle length, L/d = 3.14, tends to have slightly lower momentum fluxes than are found for the other three lengths, suggesting that  $\alpha L$  is not a complete descriptor of all damping properties.

For  $1 < \alpha L < 20$ , the reduction of  $M^+$  is roughly 70%–90% of the flow without an obstacle, which strongly depends on the damping coefficient, and the dependence becomes weaker as a further increase in the damping coefficient ( $\alpha L > 20$ ). However, the reduction of  $M^+$  reaches approximately 90% of the unobstructed flow for  $\alpha L > 100$ . This also implies that the flow resistance increases rapidly as the damping coefficient increases for obstacles with moderate damping, whereas it increases slowly for obstacles with stronger damping ( $\alpha L > 20$ ).

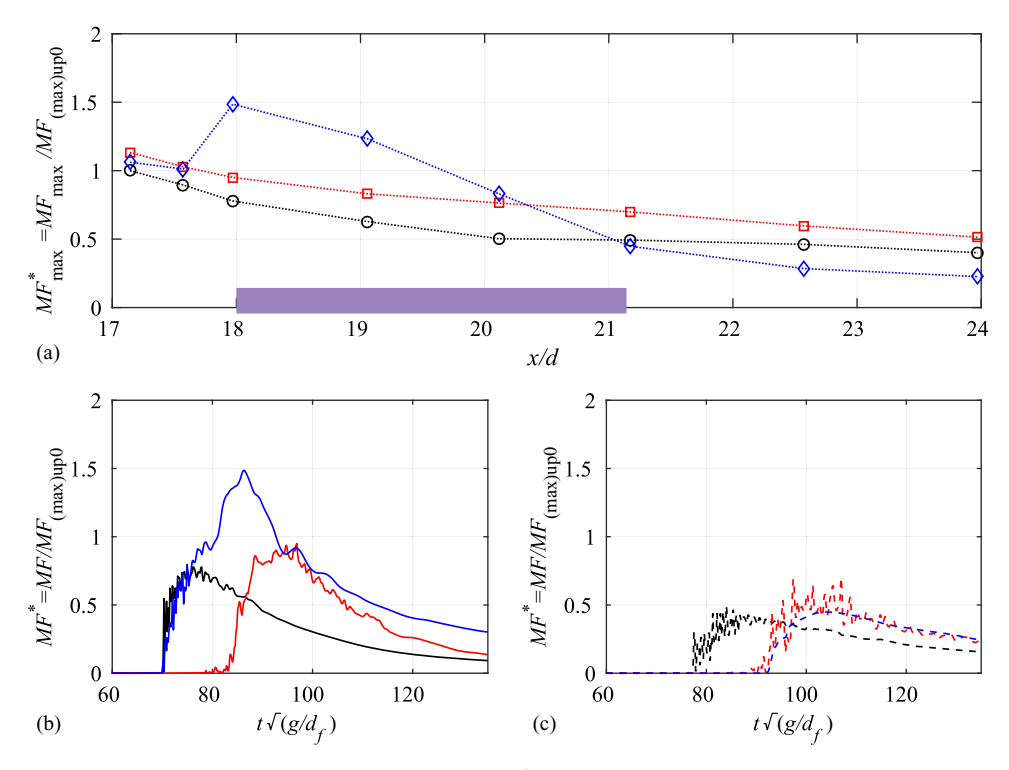


**Fig. 10.** (a) Computed nondimensionalized maximum momentum flux  $MF_{\text{max}}^*$  along the semipermeable obstacle; and time series of  $MF^*$  (b) before and (c) after obstacle for  $H_0/d = 0.26$ . The legends are the same as those defined in the caption of Fig. 7.

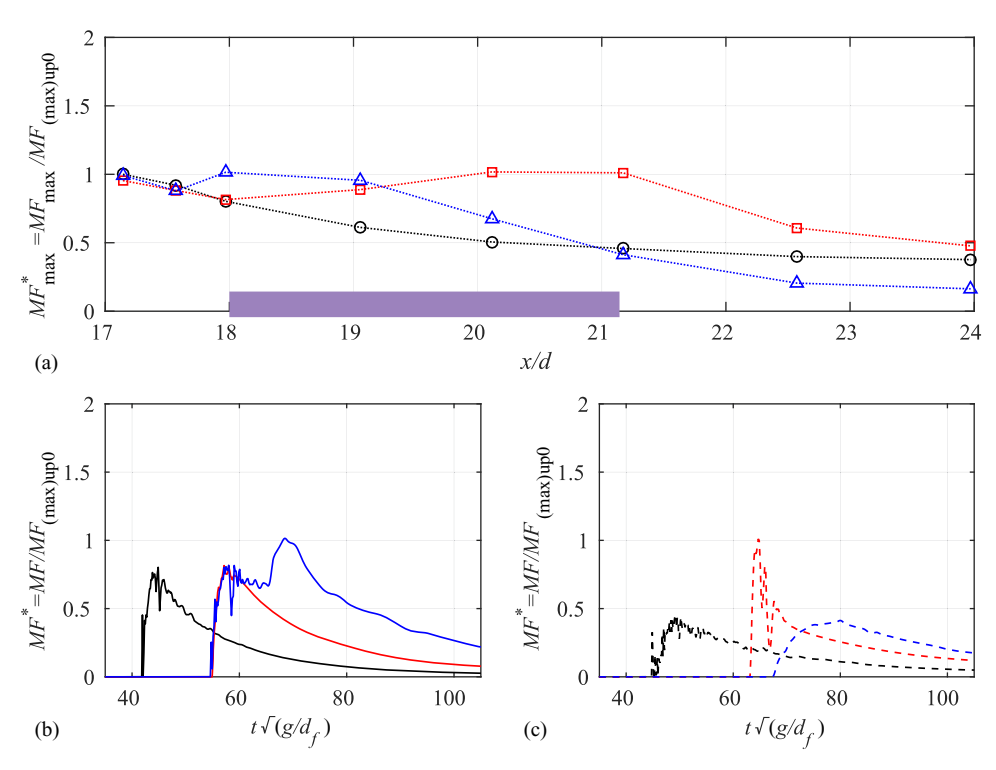


**Fig. 11.** (a) Computed nondimensionalized maximum momentum flux  $MF_{\text{max}}^*$  along the semipermeable obstacle; and time series of  $MF^*$  (b) before and (c) after obstacle for  $H_0/d = 0.49$ . The legends are the same as those defined in the caption of Fig. 7.

## Loads on a Square Cylinder

This final section of results shows the variation of runup loading on a square cylinder downstream of the semipermeable obstacle. Three wave force normalizations are used, relating conditions with the obstacle and cylinder to results that may be simpler to compute. The

first normalization  $F^* = F/MF_{CO}W$  is obtained using the maximum depth-integrated bare earth momentum flux (no obstacle, no cylinder) at the cylinder location, multiplied by the cylinder width. The bare earth momentum flux is relatively easily obtained using a variety of numerical models, and relating this to loading may prove

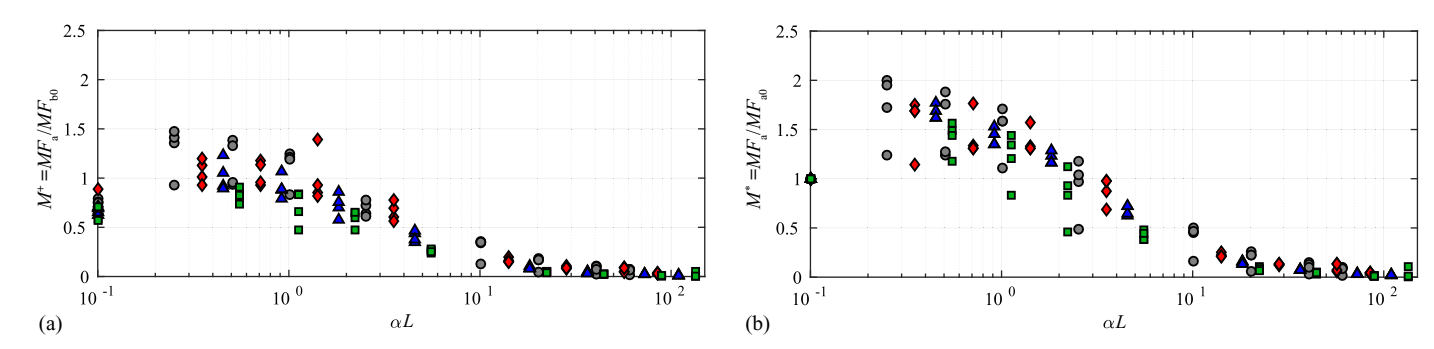


**Fig. 12.** Computed normalized maximum momentum fluxes (a)  $M^+$ ; and (b)  $M^*$  versus the normalized wave damping coefficient ( $\alpha L$ ) for four different  $H_0/d$  and L/d. Circles: L/d = 1.43; diamonds: L/d = 2.0; triangles: L/d = 2.58; squares: L/d = 3.14. Values shown at  $\alpha L = 10^{-1}$  on the log scale are actually for  $\alpha L = 0$ .

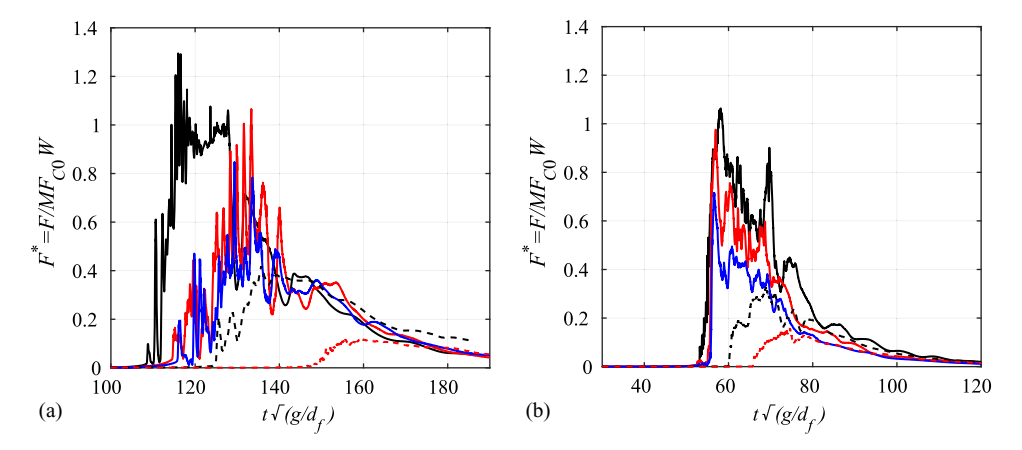


**Fig. 13.** Computed normalized wave force  $(F^* = F/MF_{C0})$  on a square cylinder versus normalized time  $(t\sqrt{g/d_f})$  for (a)  $H_0/d = 0.26$ ; and (b)  $H_0/d = 0.60$ , both for L/d = 1.43. Thick solid line:  $\alpha L = 0.0$ ; medium solid line  $\alpha L = 0.25$ ; thin solid line  $\alpha L = 2.53$ ; thick dashed line  $\alpha L = 20.26$ ; and medium dashed line  $\alpha L = 60.80$ .

useful for coastal design. Fig. 13 shows times series of these normalized loads for obstacles with five different dissipation coefficients, and for initial solitary wave heights  $H_0/d = (0.26, 0.60)$ . The first observation is clear: maximum loads decrease with increased damping coefficient,  $\alpha L$ . This decrease is visible even for the smallest damping of  $\alpha L = 0.25$ , and the decrease in loading is monotonic up to the largest damping shown,  $\alpha L = 60.8$ . This trend is very different from those for runup depth and momentum flux, both of which increased for small dissipation coefficients.

Another immediate observation is that the loads are very spiky, particularly for low or zero damping coefficients. Large variation in peak loads is a well known phenomenon in laboratory measurements, as very small variations in initial conditions and turbulence can lead to loads that may best be compared statistically, or in integrated pressure–impulse form (Peregrine 2003). For this reason, peak loads shown here should be thought of as having some error range, although it is difficult to place precise ranges on these variations. The third observation is that, because peak loads are so short-lived, load averaging over even very short time intervals may reduce their magnitudes considerably (Huang et al. 2018). Because structural systems may not respond strongly to very short-lived loads, the actual response felt by structural supports may be significantly lower than the peak.

The maximum in time of this normalized load is designated  $F_{NC0}$ , with results for all computed cases shown in Fig. 14(a). The load trend again follows a uniform pattern, decreasing with increasing  $\alpha L$ . However, there is considerable scatter: for zero damping, dimensionless loads vary between  $F_{NC0} = [0.8:1.8]$ .

By around  $\alpha L = 1$ , the upper and lower bounds have only decreased slightly to around  $F_{NC0} = [0.6:1.7]$ . However, for larger damping,  $\alpha L = 10$  to 20, the range is around  $F_{NC0} = [0.2:1.0]$ , which is a very large relative range. For  $\alpha L > 25$ , all loads show  $F_{NC0} < 0.5$ ; and  $F_{NC0} < 0.25$  for  $\alpha L > 70$ . Thus, although runup loads are reduced for large damping coefficients, significant values may still be recorded. A least-squares fit to the data is given by

$$F_{NC0} = 1.05 \cosh^{-2.30} (\log_{10}(0.69\alpha L + 1))$$
 (28)

with  $R^2 = 0.8596$  (calculated in log space). Curves are also shown for one standard deviation plus and minus in log space, which translates to curves that are  $1.5129F_{NC0}$  and  $0.6610F_{NC0}$ .

The second normalization,  $F_{NC} = F_{\text{max}}/MF_NCW$  shown in Fig. 14(b) is a transfer function between the maximum force on the cylinder and the maximum momentum flux observed at the cylinder location for the same obstacle conditions. Thus, if the maximum momentum flux is known at a structural location, the load may be estimated. This coefficient again shows considerable scatter with a range  $F_{NC} = [0.4, 2]$ , but with some structure. For the zero damping case, values are identical to  $F_{NC0}$ , with range  $F_{NC} = [0.8:1.8]$ . For  $0.2 < \alpha L < 7$ , the coefficient is notably lower than the undamped case, with range [0.4:1.6]. For damping coefficients larger than this, scatter increases greatly, with a factor of four variation in the range [0.5:2]. These results are a clear indication that, although knowledge of the momentum flux at a location

can allow loads to be computed, a considerable factor of safety may be needed. The mean value is  $F_{NC} = 1.09$  while plus and minus one standard deviation yield  $F_{NC} = [1.48, 0.71]$ . Together, these may give a basic value for computing runup loading from momentum fluxes. The final normalization  $F_{N0} = F_{\text{max}}/F_0$  shown in Fig. 14(c) is simply the ratio between the computed force on the cylinder and the corresponding load for the undamped case. This may be useful as a correction factor when undamped loads are known, but the damped loads are not. By definition, all values are unity for  $\alpha L = 0$  and, indeed,  $F_{N0} = 1$  is a reasonable upper limit for all cases for  $\alpha L \leq 1$ . As damping coefficients continue to increase, the force envelope

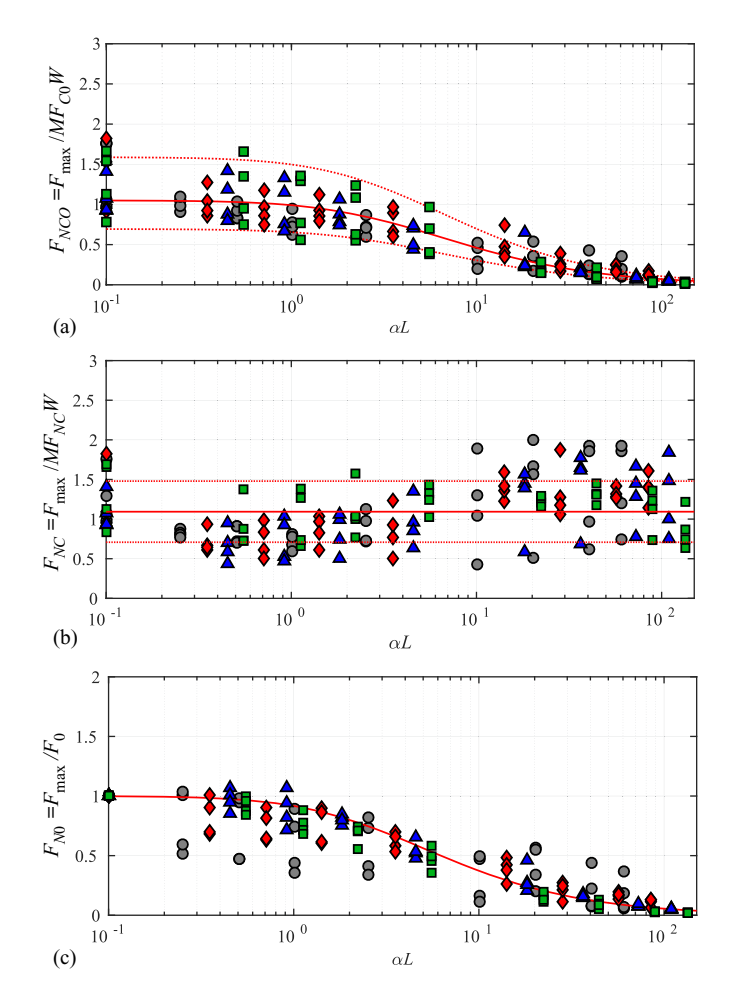


**Fig. 14.** Computed normalized wave forces (a)  $F_{NC0}$ ; (b)  $F_{NC}$ ; and (c)  $F_{N0}$  as a function of  $\alpha L$  for different  $H_0/d$  and L/d. The legends are the same as those defined in the caption of Fig. 12. Values shown at  $\alpha L = 10^{-1}$  on the log scale are actually for  $\alpha L = 0$ .

decreases monotonically, although with scatter. By  $\alpha L = 10$ , the upper envelope is around  $F_{N0} = 0.5$ , while it further decreases to below  $F_{N0} = 0.1$  by  $\alpha L = 100$ . A least-squares fit to the data is given by

$$F_{N0} = \cosh^{-2.24} \left( \log_{10} \left( 0.92\alpha L + 1 \right) \right) \tag{29}$$

with  $R^2 = 0.8524$  (calculated in log scale). Once again, this is not a fit to the envelope, so factors of safety will certainly be required. Fig. 15(a) shows the normalized wave force  $(F_{NC})$  as a function of Froude number (Fr) for all cases. Once again, although there is some scatter, considerable structure can be seen in the loads. For high Froude numbers, dimensionless loads are clearly smaller than for low Froude numbers. This appears to be because the definition of momentum flux given in Eq. (24) does not include hydrostatic loads, which would become increasingly important for lower Froude numbers. Although hydrostatic loads on the front and back sides of a cylinder act in opposite directions, and would cancel for a cylinder in a nonzero mean water depth, runup loads are different. For high Froude number runup, water arrives at the front of the structure first, and little or no water may have reached the back by the time of peak loading. This may be different for low Froude number runup, where hydrostatic loading may prove important in evaluating the net loads. Results are shown in Fig. 15(b), which includes the pressure force at the time of peak loading in the normalization, defined as  $F_{NCP} \equiv F_{max} / MF_{NCP} W$ , where

$$MF_{NCP} = \int_{-d}^{d+\eta} P + \rho u^2 dz \tag{30}$$

For high Froude numbers, the additional pressure term in Eq. (30) makes no real difference, but moderately reduces the dimensionless load 1 < Fr < 2, and greatly reduces Froude numbers for subcritical flows with Fr < 1. The mean of this dimensionless force for Fr > 1 is 1.0, which is slightly less than the one found in Fig. 14(b). Although scatter again exists, this may be used as a guideline for mean loads. Loading for subcritical runup (Fr < 1), which is likely to be less common, appears to correlate better with values computed without pressure,  $MF_{NC}$ , as loading on front and backs of structures will probably cancel to a large degree.

#### **Discussion and Conclusions**

In the present study, numerical experiments were carried out to investigate the interaction of solitary wave runup with semipermeable obstacles, and subsequent loads on a downstream cylinder using the open-source CFD models OpenFOAM and IHFOAM. The purpose of the investigation was to model wave dissipation induced by semipermeable obstacles with different properties, and the associated

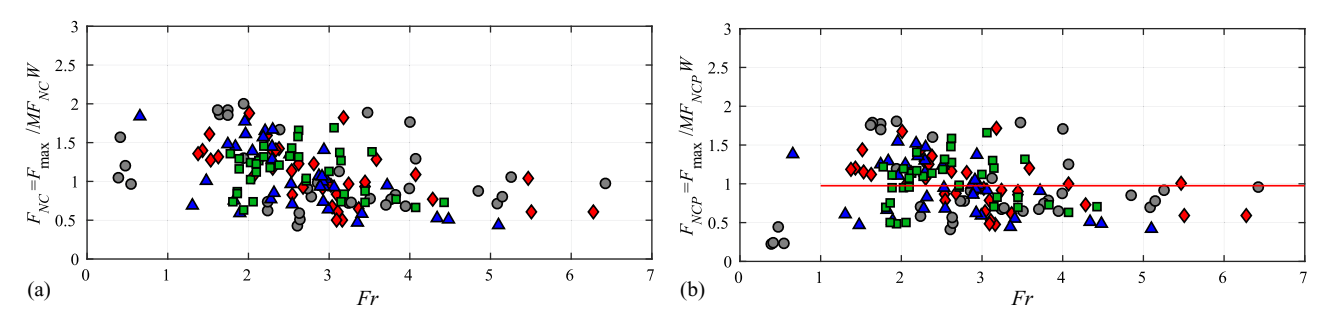


**Fig. 15.** Computed normalized wave forces (a)  $F_{NC}$ ; (b)  $F_{NCP}$  versus Fr for different cases. The legends are the same as those defined in the caption of Fig. 12.

**Table 3.** Runup damping properties for examples of semipermeable obstacles

Description	$N  ({\rm m}^{-2})$	D(m)	$C_D$	L	$\alpha L$	Reference
Dense mangroves (lower)	49	0.02	1	50	49	Massel et al. (1999)
Dense mangroves (upper)	16	0.08	1	50	64	_
Sparse mangroves (lower)	9	0.02	1	50	9	_
Sparse mangroves (upper)	1	0.08	1	50	4	_
Australian pine (Casuarina equisetifolia)	150	0.02	1	20	60	Forbes and Broadhead (2007)
Marsh grass (Spartina alterniflora)	240	0.012	1	20	58	Morgan et al. (2005)
	608	0.012	1	20	146	_
Pile breakwater	0.125	2	1	12	3	Koftis et al. (2012)
	411	0.035	1	13	4.3	Belibassakis et al. (2018)

wave forces on a downstream cylinder. A total of 276 simulations were performed for a wide range of different damping coefficients. For almost all nonzero damping coefficients tested, runup heights were amplified at both the upstream and downstream ends of the obstacle, compared with the bare earth case. This appeared to be because of partial reflection of the runup, and because supercritical flows tend to increase in depth when they lose energy. The dependence of runup depth on damping properties was relatively weak. In contrast, the variation of momentum flux showed a strong dependence on the damping coefficient, with a general decrease in peak flux for  $\alpha L > 2$ , but with generally increased peak momentum flux for  $\alpha L \leq 1$ . This increase in momentum flux for low damping appeared to be related to the corresponding increase in runup height. However, loads on a downstream square cylinder were found to decrease monotonically when compared with the no obstacle case. Peak loads were found to be closely related to peak momentum flux (with several definitions), but with considerable scatter. Part of the variation may be inherent in evaluating shortlived turbulent loads, but some may also be related to other factors not considered here.

Dissipation of wave runup by semipermeable vegetation or cylinders clearly differs from that expected for waves traveling over a larger mean water depth. The damping coefficient  $\alpha L$  adapted from Mendez and Losada (2004) was considered as the measure of dissipation, and proved useful. This may be evaluated for many natural and constructed obstacles, as shown in Table 3 for five relevant practical cases. The first case refers to both dense and sparse coastal forests composed of rhizophora (mangrove) species in Iriomote Island, Japan (Massel et al. 1999). The dense coastal forest acts as a barrier and protects the coast from large storm waves and tsunamis. The second case corresponds to dense coastal vegetation with Casuarina equisetifolia (Australian pine) species in Banda Aceh, Indonesia (Forbes and Broadhead 2007). Example 3 shows typical properties of coastal wetlands with Spartina alterniflora plant species. The final examples refer to a multiple-row pile breakwaters. Damping coefficients have a large range, reaching the very high value of  $\alpha L = 146$  for *S. alterniflora* marsh grass, although the present work will probably overestimate damping for highly flexible vegetation. Dense mangroves also have a reasonably large damping, although here it is also uncertain whether a single stem density will suffice to represent damping. Overall results show that, in many cases, obstacle induced damping may be sufficient to significantly reduce loads.

For practical purposes, this work provided several methods to evaluate runup loads behind obstacles, all summarized in Fig. 14. If bare earth momentum fluxes are known at the structure location, Eq. (28) will estimate the structural loading behind a semipermeable obstacle from a knowledge of  $\alpha L$ . If damped momentum fluxes (where no damping is included as a special case) are known at any structural location, results here suggest that  $F_{NC}$  = 1.09 is a mean value using peak momentum fluxes defined without pressures as

in Eq. (24), or  $F_{NCP}$  = 1.00 using momentum fluxes defined with pressure as in Eq. (30). The latter result should only be used for supercritical runup. When structural loads are known for the undamped case, Eq. (29) provides a reduction factor based on the present simulations. Once again, it should be noted that all of these loads show considerable scatter, so factors of safety will be required.

All work performed here was for structures behind two-dimensional emergent obstacles, which may not be a reasonable approximation for many real-world situations with finite obstacle lengths, complex 3D shapes, or for submerged obstacles. Work continues on many of these topics, and will be reported on soon.

## **Data Availability Statement**

All data, models, and code generated or used during the study are available from the corresponding author by request.

## **Acknowledgments**

Work for this paper was funded by a grant from the National Institute of Standards and Technology, and by the National Science Foundation (grant number CMMI-1727662). Their support is gratefully acknowledged. The authors also acknowledge the computing time granted through NHERI DesignSafe.

## **Notation**

The following symbols are used in this paper:

 $C_D = \text{drag force coefficient};$ 

D = diameter of a stem;

d = offshore water depth;

d<sub>f</sub> = water depth immediately after the semipermeable obstacle at the time of maximum momentum flux;

 $F_{\text{max}}$  = maximum horizontal force on a square cylinder with obstacle in place;

 $F_0$  = maximum horizontal force on a square cylinder with no obstacle;

 $H_a = \eta_{\text{max}}$  immediately after the obstacle;

 $H_b = \eta_{\text{max}}$  immediately before the obstacle;

 $H_{a0} = \eta_{\text{max}}$  immediately after the obstacle location for the bare earth case ( $\alpha L = 0$ , with no cylinder present);

 $H_{b0} = \eta_{\text{max}}$  immediately before the obstacle for the bare earth case ( $\alpha L = 0$ , with no cylinder present);

 $H_0$  = offshore wave height;

L =obstacle length;

MF = momentum flux (not including pressure component);

 $MF_a = MF_{\text{max}}$  immediately after the obstacle;

- $MF_{a0} = MF_{\text{max}}$  immediately after the semipermeable obstacle for the bare earth case ( $\alpha L = 0$ , with no cylinder present);
- $MF_{b0} = MF_{\text{max}}$  immediately before the obstacle for the bare earth case ( $\alpha L = 0$ , with no cylinder present);
- $MF_{c0} = MF_{\text{max}}$  at the cylinder location for the bare earth case ( $\alpha L = 0$ , with no cylinder present);
- $MF_{\text{max}} = \text{maximum momentum flux};$
- $MF_{NC} = MF_{\text{max}}$  at the cylinder location for the obstructed flow (not including pressure component, with no cylinder present);
- $MF_{NCP} = MF_{\text{max}}$  at the cylinder location for the obstructed flow (including pressure component, with no cylinder present);
  - N = number of stems per unit horizontal area in the semipermeable obstacle;
  - P = hydrostatic pressure;
  - W = cylinder width;
  - $\eta$  = water surface elevation;
  - $\eta_{\text{max}} = \text{maximum water surface elevation; and}$
- $\eta_{(\text{max})\text{up0}} = \text{maximum surface elevation at } 0.86d \text{ shoreward}$ from the edge of the crest for the bare earth case.

#### References

- Alagan Chella, M., H. Bihs, D. Myrhaug, and M. Muskulus. 2016. "Hydrodynamic characteristics and geometric properties of plunging and spilling breakers over impermeable slopes." *Ocean Modell*. 103: 53–72. https://doi.org/10.1016/j.ocemod.2015.11.011.
- Anderson, M. E., and J. M. Smith. 2014. "Wave attenuation by flexible, idealized salt marsh vegetation." *Coastal Eng.* 83: 82–92. https://doi.org/10.1016/j.coastaleng.2013.10.004.
- Augustin, L. N., J. L. Irish, and P. Lynett. 2009. "Laboratory and numerical studies of wave damping by emergent and near-emergent wetland vegetation." *Coastal Eng.* 56 (3): 332–340. https://doi.org/10.1016/j.coastaleng .2008.09.004.
- Belibassakis, K. A., G. Arnaud, V. Rey, and J. Touboul. 2018. "Propagation and scattering of waves by dense arrays of impenetrable cylinders in a waveguide." *Wave Motion* 80: 1–19. https://doi.org/10.1016/j.wavemoti.2018.03.007.
- Blackmar, P. J., D. T. Cox, and W. C. Wu. 2014. "Laboratory observations and numerical simulations of wave height attenuation in heterogeneous vegetation." *J. Waterway, Port, Coastal, Ocean Eng.* 140 (1): 56–65. https://doi.org/10.1061/(ASCE)WW.1943-5460.0000215.
- Chakrabarti, A., Q. Chen, H. D. Smith, and D. Liu. 2016. "Large eddy simulation of unidirectional and wave flows through vegetation." *J. Eng. Mech.* 142 (8): 04016048. https://doi.org/10.1061/(ASCE)EM.1943-7889.0001087.
- Chen, Q., and H. Zhao. 2012. "Theoretical models for wave energy dissipation caused by vegetation." J. Eng. Mech. 138 (2): 221–229. https://doi.org/10.1061/(ASCE)EM.1943-7889.0000318.
- Chen, X., Q. Chen, J. Zhan, and D. Liu. 2016. "Numerical simulations of wave propagation over a vegetated platform." *Coastal Eng.* 110: 64–75. https://doi.org/10.1016/j.coastaleng.2016.01.003.
- Dalrymple, R. A., J. T. Kirby, and P. A. Hwang. 1984. "Wave diffraction due to areas of energy dissipation." *J. Waterway, Port, Coastal, Ocean Eng.* 110 (1): 67–79. https://doi.org/10.1061/(ASCE)0733-950X(1984) 110:1(67).
- Dalrymple, R. A., S. N. Seo, and P. A. Martin. 1988. "Water wave scattering by rows of circular cylinders." In *Proc.*, 21st Int. Conf. on Coastal Engineering, 2216–2228. Costa del Sol-Malaga, Spain. https://ascelibrary.org/doi/abs/10.1061/9780872626874.165.
- Dubi, A., and A. Torum. 1994. "Wave damping by kelp vegetation." In Vol. 1 of *Proc.*, 24th Int. Conf. on Coastal Engineering, 142–156. Kobe, Japan. https://icce-ojs-tamu.tdl.org/icce/index.php/icce/article/view/4952.

- Forbes, K., and J. Broadhead. 2007. *The role of coastal forests in the mitigation of tsunami impacts*. Rep. No. 2007/1. Rome, Italy: Food and Agriculture Organization of the United Nations.
- Henry, P. Y., and D. Myrhaug. 2013. "Wave-induced drag force on vegetation under shoaling random waves." *Coastal Eng.* 78: 13–20. https://doi.org/10.1016/j.coastaleng.2013.03.004.
- Hiraoka, H., and M. Ohashi. 2008. "A  $(k-\epsilon)$  turbulence closure model for plant canopy flows." *J. Wind Eng. Ind. Aerodyn.* 96 (10–11): 2139–2149. https://doi.org/10.1016/j.jweia.2008.02.018.
- Hirt, C. W., and B. D. Nichols. 1981. "Volume of fluid (VOF) method for the dynamics of free boundaries." *J. Comput. Phys.* 39 (1): 201–225. https://doi.org/10.1016/0021-9991(81)90145-5.
- Hu, Z., T. Suzuki, T. Zitman, W. Uittewaal, and M. Stive. 2014. "Laboratory study on wave dissipation by vegetation in combined current-wave flow." *Coastal Eng.* 88: 131–142. https://doi.org/10.1016/j.coastaleng.2014.02.009.
- Huang, M., A. B. Kennedy, T. Tomiczek, and J. J. Westerink. 2018. "Solitary wave impacts on vertical and overhanging near-coast structures." *Coastal Eng. J.* 60 (3) 356–370. https://doi.org/10.1080/21664250.2018.1542963.
- Huang, Z., Y. Yao, S. Y. Sim, and Y. Yao. 2011. "Interaction of solitary waves with emergent, rigid vegetation." *Ocean Eng.* 38 (10): 1080– 1088. https://doi.org/10.1016/j.oceaneng.2011.03.003.
- Kakuno, S., and Y. Nakata. 1998. "Scattering of water waves by rows of cylinders with/without a backwall." Appl. Ocean Res. 20 (4): 191– 198. https://doi.org/10.1016/S0141-1187(97)00026-6.
- Kathiresan, K., and N. Rajendran. 2005. "Coastal mangrove forests mitigated tsunami." *Estuarine Coastal Shelf Sci.* 65 (3): 601–606. https://doi.org/10.1016/j.ecss.2005.06.022.
- Kobayashi, N., A. W. Raichle, and T. Asano. 1993. "Wave attenuation by vegetation." J. Waterway, Port, Coastal, Ocean Eng. 119 (1): 30–48. https://doi.org/10.1061/(ASCE)0733-950X(1993)119:1(30).
- Koftis, T., P. Prinos, and M. Aftias. 2012. "Experimental study of a multiple-row pile breakwater." In Proc., 4th Int. Conf. on the Application of Physical Modelling to Port and Coastal Protection. Ghent University: Ghent, Belgium. http://documentatiecentrum.watlab .be/imis.php?module=conference&confid=2476.
- Lee, J., J. Skjelbreia, and F. Raichlen. 1982. "Measurement of velocities in solitary waves." J. Waterway, Port, Coastal, Ocean Div. 108 (2): 200–218.
- Lin, P. 2008. Numerical modeling of water waves. Boca Raton, FL: CRC Press.
- Løvås, S. M., and A. Tørum. 2001. "Effect of the kelp *Laminaria hyperborea* upon sand dune erosion and water particle velocities." *Coastal Eng.* 44 (1): 37–63. https://doi.org/10.1016/S0378-3839(01)00021-7.
- Ma, G., J. T. Kirby, S. F. Su, J. Figlus, and F. Shi. 2013. "Numerical study of turbulence and wave damping induced by vegetation canopies." *Coastal Eng.* 80: 68–78. https://doi.org/10.1016/j.coastaleng.2013.05.007.
- Massel, S. R., K. Furukawa, and R. Brinkman. 1999. "Surface wave propagation in mangrove forests." *Fluid Dyn. Res.* 24 (4): 219–249. https://doi.org/10.1016/S0169-5983(98)00024-0.
- Maza, M., J. L. Lara, and I. J. Losada. 2013. "A coupled model of submerged vegetation under oscillatory flow using Navier–Stokes equations." *Coastal Eng.* 80: 16–34. https://doi.org/10.1016/j.coastaleng.2013.04.009.
- Maza, M., J. L. Lara, and I. J. Losada. 2015. "Tsunami wave interaction with mangrove forests: A 3-D numerical approach." *Coastal Eng.* 98: 33–54. https://doi.org/10.1016/j.coastaleng.2015.01.002.
- Maza, M., J. L. Lara, and I. J. Losada. 2016. "Solitary wave attenuation by vegetation patches." Adv. Water. Resour. 98: 159–172. https://doi.org /10.1016/j.advwatres.2016.10.021.
- Mei, C. C., I.-C. Chan, P. L.-F. Liu, Z. Huang, and W. Zhang. 2011. "Long waves through emergent coastal vegetation." J. Fluid Mech. 687: 461– 491. https://doi.org/10.1017/jfm.2011.373.
- Mendez, F. J., and I. J. Losada. 2004. "An empirical model to estimate the propagation of random breaking and nonbreaking waves over vegetation fields." *Coastal Eng.* 51 (2): 103–118. https://doi.org/10.1016/j .coastaleng.2003.11.003.
- Méndez, F. J., I. J. Losada, and M. A. Losada. 1999. "Hydrodynamics induced by wind waves in a vegetation field." J. Geophys. Res. Oceans 104 (C8): 18383–18396. https://doi.org/10.1029/1999JC900119.
- Morgan, P. A., L. Curci, C. Dalton, and J. Miller. 2005. Assessing the health of fringing salt marshes along the fore river and its tributaries. Environmental

- Studies Faculty Publications 1. Armidale, NSW: University of New England.
- Myrhaug, D., and L. E. Holmedal. 2011. "Drag force on a vegetation field due to long-crested and short-crested nonlinear random waves." *Coastal Eng.* 58 (6): 562–566. https://doi.org/10.1016/j.coastaleng.2011.01.014.
- Nepf, H. M. 1999. "Drag, turbulence, and diffusion in flow through emergent vegetation." Water Resour. Res. 35 (2): 479–489. https://doi.org/10.1029/1998WR900069.
- Peregrine, D. 2003. "Water-wave impact on walls." *Annu. Rev. Fluid Mech.* 54: 23–43. https://doi.org/10.1146/annurev.fluid.35.101101.161153.
- Peruzzo, P., F. de Serio, A. Defina, and M. Mossa. 2018. "Wave height attenuation and flow resistance due to emergent or near-emergent vegetation." Water 10 (4): 402. https://doi.org/10.3390/w10040402.
- Richardson, L. F., and J. A. Gaunt. 1927. "VIII. The deferred approach to the limit." *Philos. Trans. R. Soc. London, Ser. A* 226 (636–646): 299–361.
- Roache, P. J. 1994. "Perspective: A method for uniform reporting of grid refinement studies." J. Fluids Eng. 116 (3): 405–413. https://doi.org /10.1115/1.2910291.
- Shuto, N. 1987. "The effectiveness and limit of tsunami control forests." Coastal Eng. Jpn. 30 (1): 143–153. https://doi.org/10.1080/05785634 .1987.11924470.

- Stoesser, T., G. P. Salvador, W. Rodi, and P. Diplas. 2009. "Large eddy simulation of turbulent flow through submerged vegetation." *Transp. Porous Media* 78 (3 SPEC. ISS.): 347–365. https://doi.org/10.1007/s11242-009-9371-8.
- Svendsen, I. A. 1978. "Wave characteristics in the surf zone." In *Proc.*, 16th Conf. on Coastal Engineering, 520–539. Hamburg, Germany. https://doi.org/10.1061/9780872621909.031.
- Tanino, Y., and H. M. Nepf. 2008. "Laboratory investigation of mean drag in a random array of rigid, emergent cylinders." *J. Hydraul.* Eng. 134 (1): 34–41. https://doi.org/10.1061/(ASCE)0733-9429(2008) 134:1(34).
- Vo Luong, P., and S. Massel. 2008. "Energy dissipation in non-uniform mangrove forests of arbitrary depth." *J. Mar. Syst.* 74 (1-2): 603–622. https://doi.org/10.1016/j.jmarsys.2008.05.004.
- Wiegel, R. L. 1961. Closely spaced piles as a breakwater. Rep. No. S140 I6. Berkeley, CA: University of California, Hydraulic Engineering Laboratory.
- Yang, Y., J. L. Irish, and R. Weiss. 2017. "Impact of patchy vegetation on wave and runup dynamics." J. Waterway, Port, Coastal, Ocean Eng. 143 (4): 1–16. https://doi.org/10.1061/(ASCE)WW.1943-5460 .0000380.